Supporting Information

Heteroatoms Induce Localization of the Electric Field and Promote a Wide Potential-Window Selectivity Towards CO in the CO_2 Electroreduction

C. Cai, B. Liu, K. Liu, P. Li, J. Fu, Y. Wang, W. Li, C. Tian*, Y. Kang, A. Stefancu, H. Li, C.-W. Kao, T.-S. Chan, Z. Lin, L. Chai, E. Cortés*, M. Liu*

Experimental Section

Chemicals. Chemicals

Sodium hydroxide (≥96%, Shanghai Chemical Reagents, China), Sliver nitrate (≥ 99.8%, Aladdin), Tin chloride dihydrate (≥ 96%, Aladdin) Potassium bicarbonate (99.5%, Aladdin), Sodium borohydride (98%, Aladdin) deionized water (18.2 MΩ), and Nafion solution (5 wt.%, D-520) were used no further purification. Carbon paper (TGP-H-060) was used as the cathode substrate.

Sample preparation

The Ag/Sn nanoparticle was synthesized by a coprecipitation reduction. In detail, 1 mol $SnCl_2.2H_2O$ and a volume of 5 mL sliver nitrate solution (1 M) $AgNO_3$ was added in(a)volume of 80 mL deionized water in turn. Then, a volume of 7 mL sodium hydroxide solution (1 M) was dropped in the mixture solution under stirring to enable a homogenous mixture. Last, 10 ml sodium borohydride solution (0.2 g) was added into the above solution very slowly. Finally, the product was collected after centrifugation and vacuum drying at ~30 °C. Ag nanoparticles were prepared by the same way, but without $SnCl_2.2H_2O$.

Electrode preparation for GFC.

The electrode inks were prepared as follow. 10 mg Pristine catalyst powder was added into a mixture solution with 500μL deionized water, 500μL absolute alcohol and 60μL Nafion solution (5wt%), ultrasound 30 min until the mixture solution becomes the homogeneous solution. After that, the above solution was dropped on the prepared electrode, and the loading of catalyst on the electrode was ~0.5 mg cm^{-2}.

CO₂RR performance measurements and product analysis.

Electrochemical tests were carried out with a workstation (PG302N+BA) at room temperature. The electrolysis experiments were performed by(a)H-cell reactor with a Nafion-117 membrane to segregate cathodic chamber and anodic chamber. In the cathodic chamber (50 mL), an SGL carbon paper and Ag/AgCl treated as the working and reference electrode, respectively. Pt foil in the anodic chamber (50 mL) as a counter electrode. Each chamber contained 30 mL $KHCO_3$ (99.5%, Aladdin) electrolyte (0.1 M, pH = 6.8). Carbon dioxide was continuously purged (20 mL min^{-1}, 99.999%) during the ECR process. All potentials were recalculated into by (1)

$$E_{RHE}=E_{Ag/AgCl}+ 0.1989 +0.0592\times pH \qquad (1)$$

and iR compensation was also taken into consideration.

As the gas flow cell test, a commercial anion exchange membrane (FAA-PK-130) separates the as-prepared cathodic gas diffusion electrode (GDE) with geometric active area of 1 cm^2 from the anode. Nickel foam worked as the anode, and Ag/AgCl electrode served as the reference electrode. A peristaltic pump (BT100M, Longer) circulates 1 M KOH electrolyte (~50 mL) continuedly. A 20 mL amount of electrolyte (1 M KOH, pH = 14) was circulated through both the anode and cathode chambers by two pumps with

a flow rate of 10 mL min^{-1}. Meanwhile, CO_2 gas was continuously supplied to the gas chamber located at the back side of the cathode by using a mass flow controller with a flow rate of 20 mL min^{-1}. The performance of the cathodes was evaluated by performing constant-current electrolysis.

Characterizations
Scanning electron microscope (SEM) images were obtained from a FEI Helios Nanolab 600 field emission electron microscope. Transmission electron microscopy (TEM) was conducted on(a)Titan G 260 – 300 microscopes with probe corrector. Powder X-ray diffraction (XRD) patterns were collected using a D8 advance X-ray diffractometer (Rigaku, Japan) with Cu Kα radiation (λ = 0.15406 nm) at a scan rate (2 θ) of 0.05-degree s^{-1}. X-ray photoelectron spectroscopy (XPS) measurements were performed on Thermo Fisher Scientific-K-Alpha^{+}, and all the binding energies were calibrated by the C 1s peak at 284.3 eV. Nitrogen adsorption desorption isotherms were obtained on Micromeritics ASAP 2020 nitrogen adsorption apparatus. Brunauer–Emmett–Teller (BET) surface areas were calculated by a multipoint BET method using adsorption data at the relative pressure (P/P_0) range 0.05 – 0.3. Thermofisher Scientific Themis Z Cs-corrected transmission electron microscope at 300 kV. The Ag K-edge X-ray absorption near edge structure (XANES) and extended X-ray absorption fine structure (EXAFS) spectra were recorded with a beamline 01C1 at the National Synchrotron Radiation Research Center (NSRRC), Hsinchu, Taiwan, operated at 1.5 GeV with a current of 360 mA. The Raman was conducted on inVia Reflex (made by Renishaw, UK), using laser with wavenumber of 533 nm and power of 100 mW. During test, the carbon supported Ag/Sn alloy, Pt wire and Ag/AgCl are used as working electrode support, counter electrode and reference electrode, respectively.
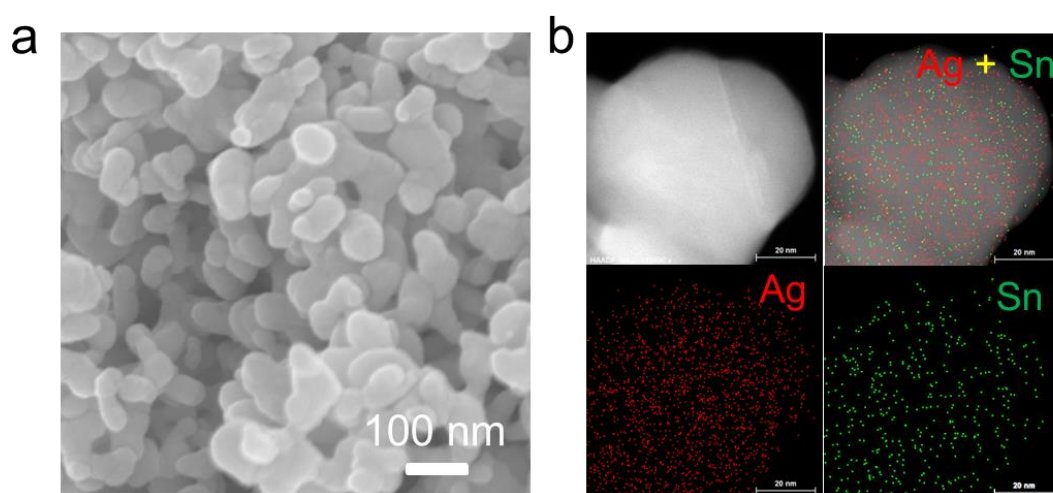
Supplementary Figures

a

100 nm

b

Figure S1 Characterizations of the Ag/Sn catalyst. (a) SEM image. (b) HAADF-STEM image and corresponding EDS element mapping**.**
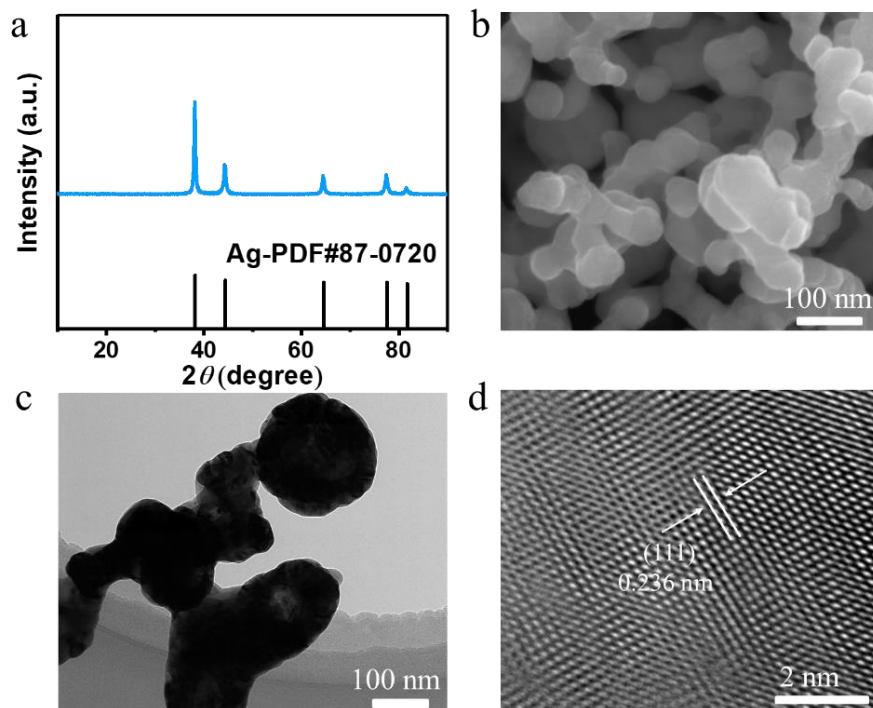
Figure S2 Characterizations of the Ag catalyst. (a) XRD pattern. (b) SEM image. (c) Typical TEM image. (d) HRTEM image.
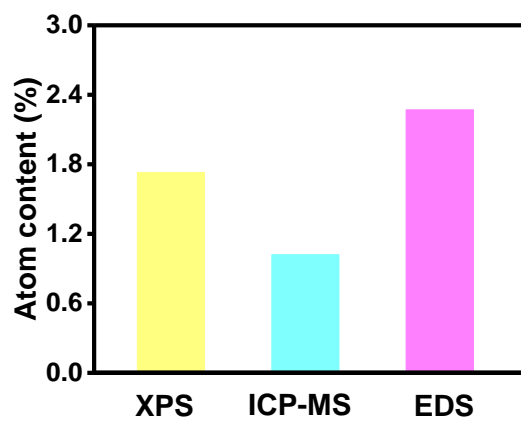
Figure S3 The Sn contents of Ag /Sn catalyst. The Sn atom content were illustrated by, ICP-MS, XPS spectrum and EDX analysis.
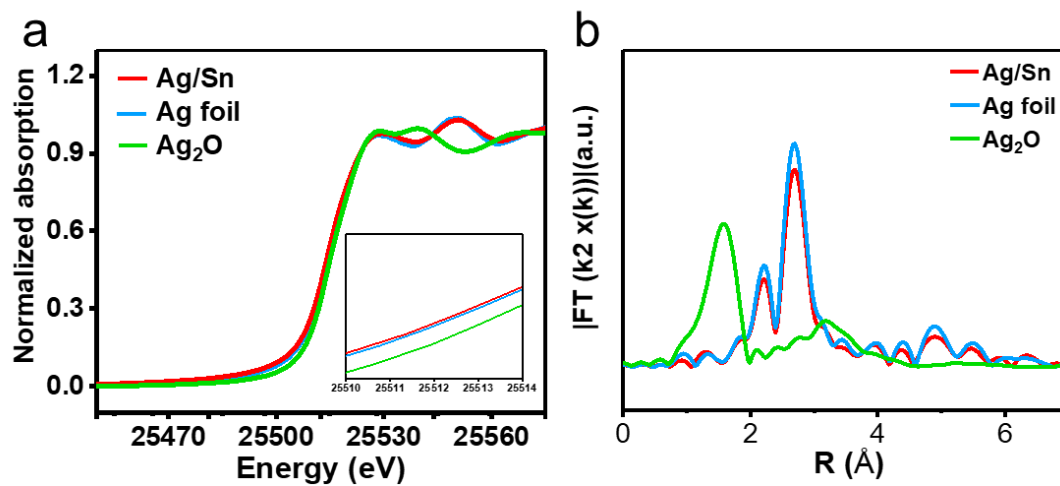
Figure S4 Chemical environment and electron density transfer analysis. (a) Ag K-edge XANES, and (b) corresponding Fourier-transform K^2-weighted EXAFS spectra.
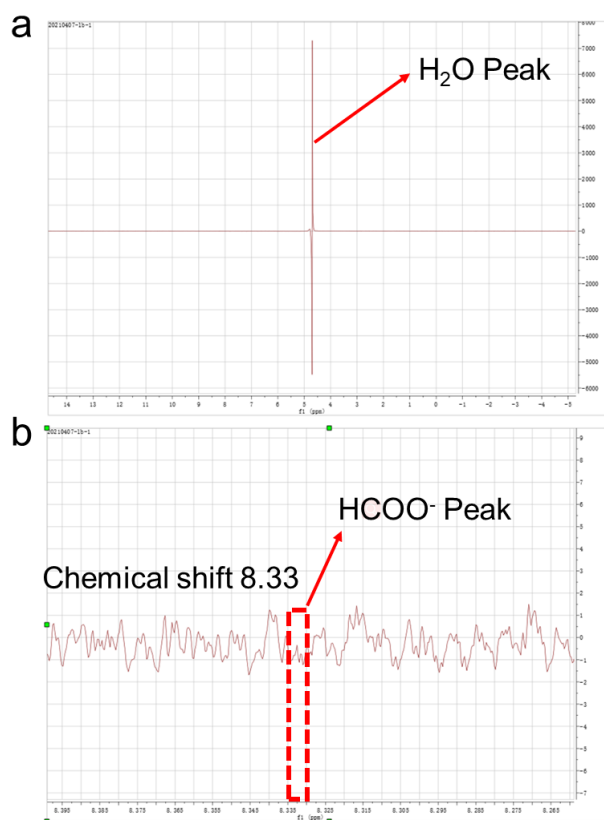
a

H₂O Peak

b

HCOO⁻ Peak

Chemical shift 8.33

Figure S5 1H 1D NMR spectrum of Ag/Sn during CO₂RR in 0.1M KHCO₃. The assignment is based on Kuhl, Energy Environ. Sci., 2012, 5, 7050-7059.
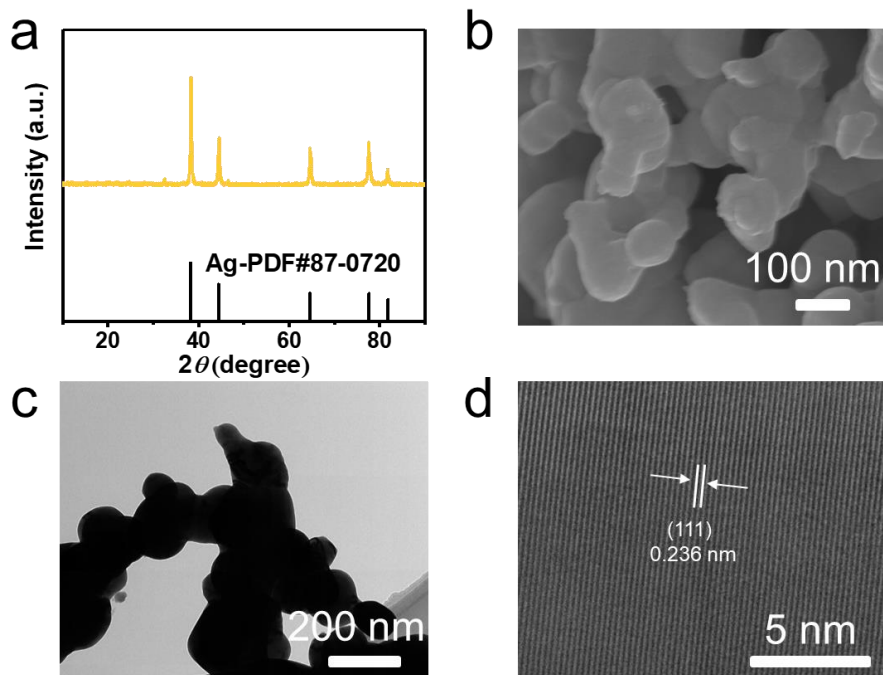
Figure S6 Characterizations of the Ag/Sn HCl catalyst. (a) XRD pattern. (b) SEM image. (c) Typical TEM image. (d) HRTEM image.
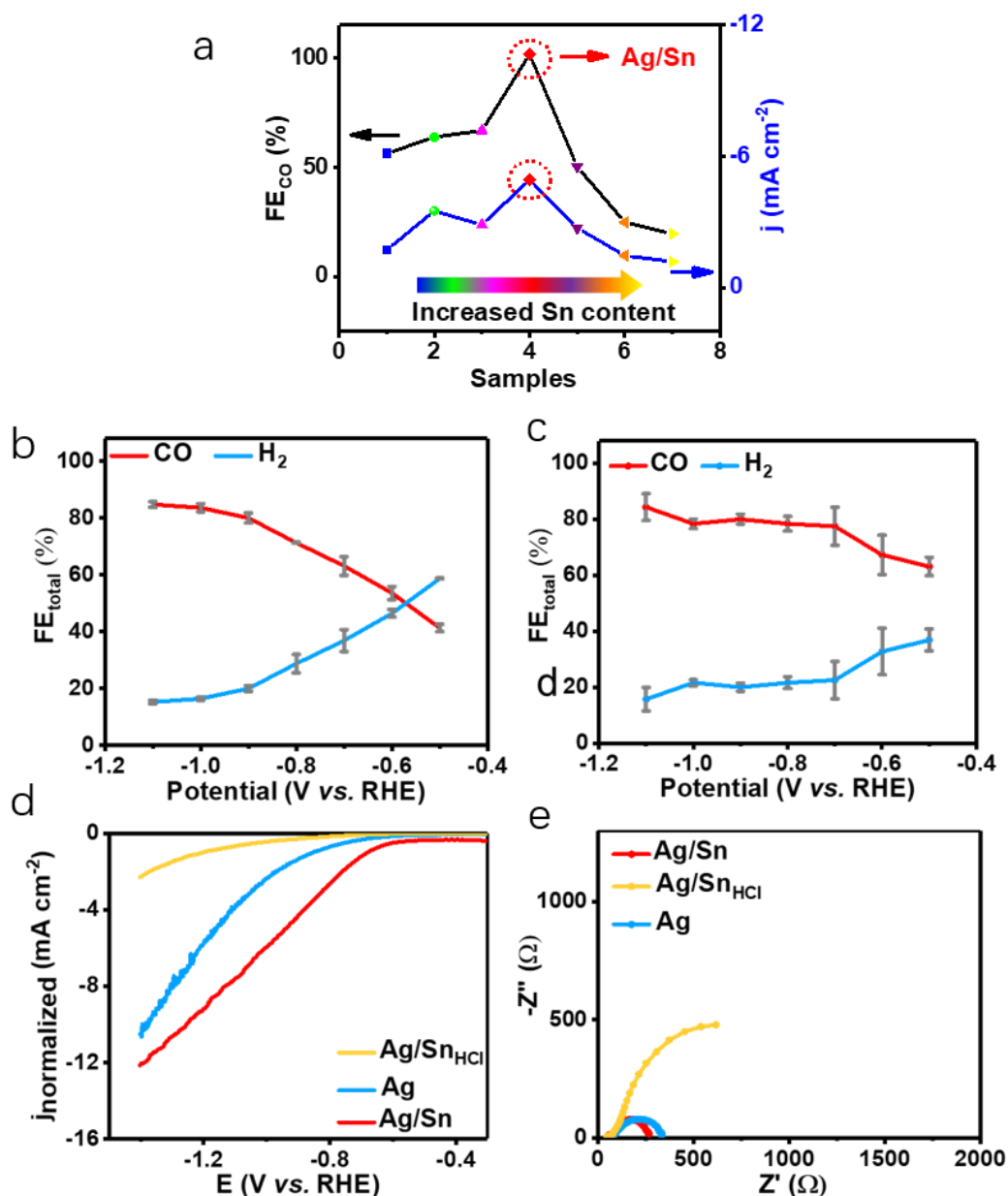
Figure S7 ECR performance of catalysts. (a) the ratio dependent activity test of Ag/Sn alloy. (b) Total FE of Ag. (c) Total FE of Ag/Sn $_{HCl}$. (d) Current density was normalized by electrochemical surface area. (e) Electrochemical impedance spectra (EIS). The Nyquist plots were measured with frequencies ranging from 100 kHz to 0.1 Hz at a potential of -1 V (versus RHE) in H-cell system. The catalytic performance of Ag/Sn alloy is sensitive to the Ag/Sn ratio. The Ag/Sn alloy with ratio of 96:4 possesses the highest FE$_{CO}$ to ~100% and the largest density of ~8 mA/cm^2 among those synthesized samples.
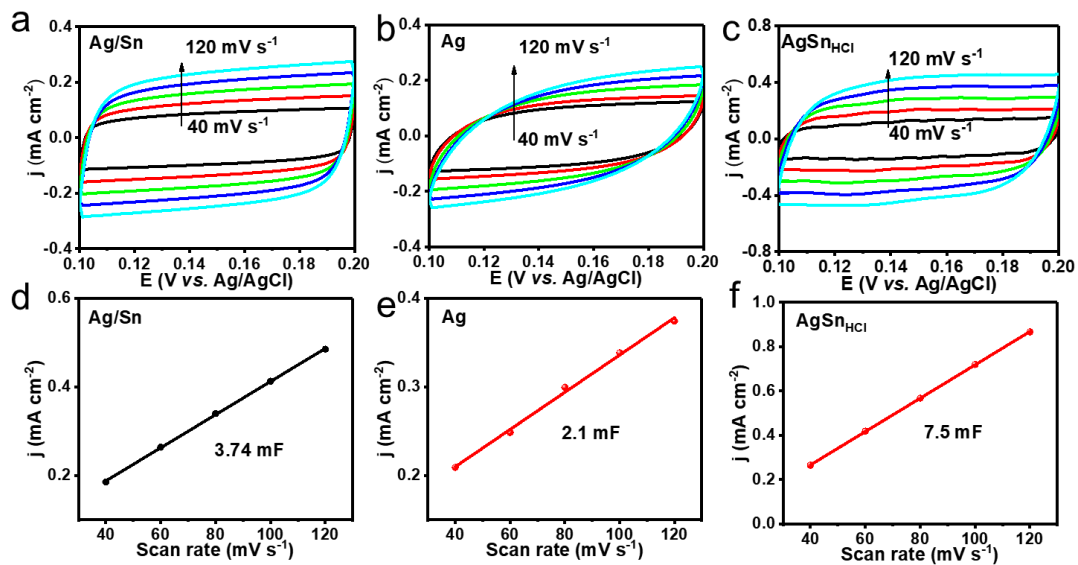
Figure S8 ECSA estimation determined from C _dl._ CVs of Ag/Sn (a), Ag (b) and Ag/Sn _HCl_ (c) at a range of 0.1 V and -0.2 V *vs.* Ag/AgCl without faraday reaction. The scan rates are set as 40, 60, 80, 100, and 120 mV s-1. Linear fitting of the capacitive currents versus scan rates for Ag/Sn (d), Ag (e) and Sn (f) electrocatalysts.
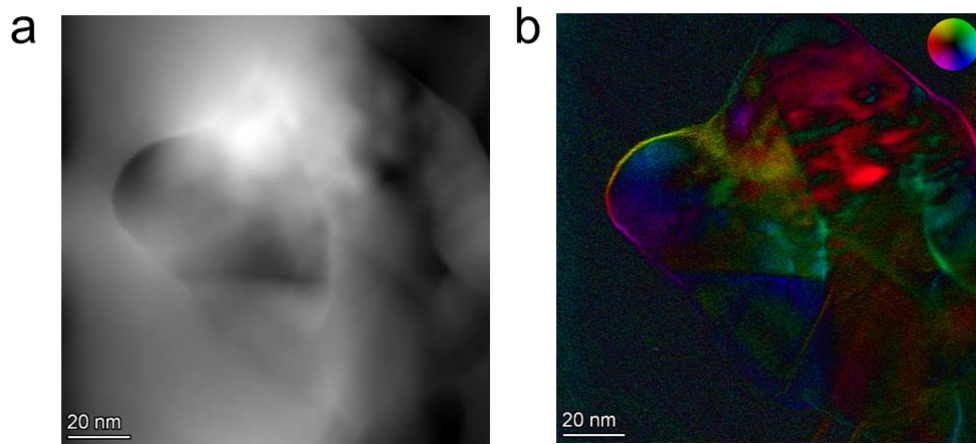
a

b

Figure S9 Differential phase contrast (DPC) STEM images of Ag/Sn catalyst after CO₂RR test.
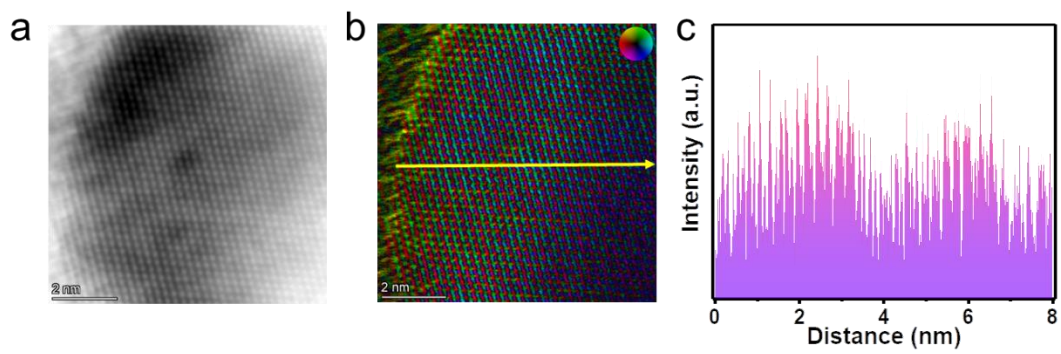
Figure S10 Characterizations of the Ag/Sn catalyst after CO₂RR. (a) HR-STEM image. (b) Arrow-map representations of strength and orientation of electric field. (c) Linear profile.
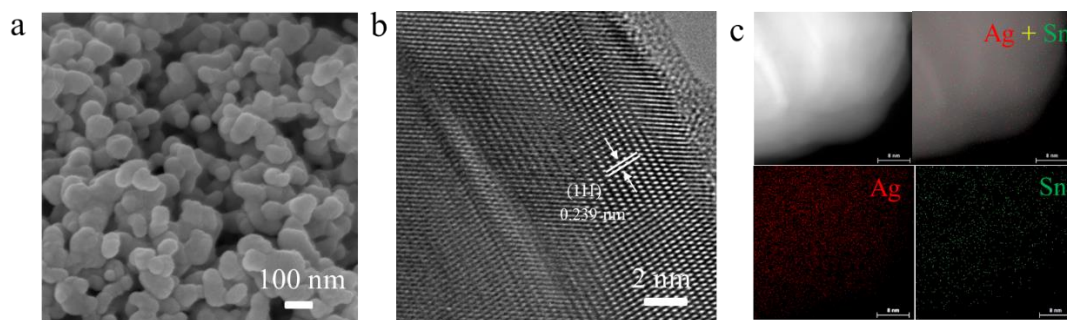
Figure S11 Characterizations of the Ag/Sn catalyst after reduction. (a) SEM image. (b) HR-TEM image. (c) Corresponding EDS element mapping.
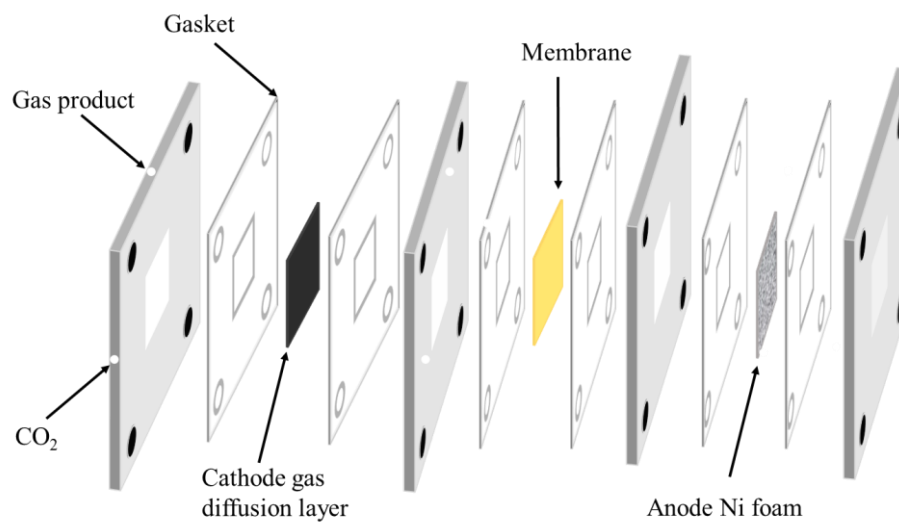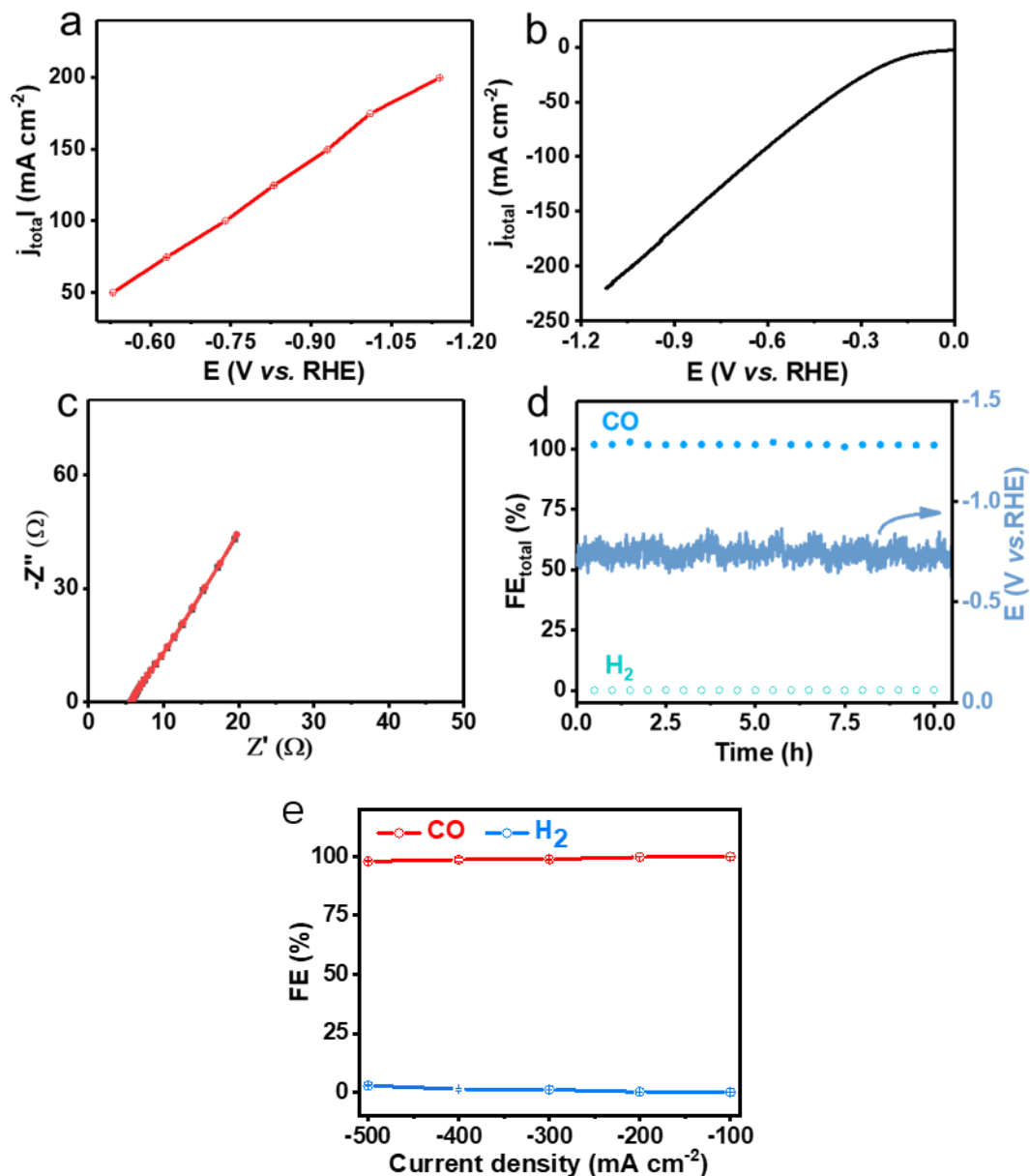
Figure S12 Schematic illustration of gas flow cell.

.

Figure S13 ECR performance of catalysts. (a) Partial CO current densities j $_{CO}$ versus potentials referred to the reversible hydrogen electrode (RHE) on Ag/Sn catalysts. (b) Linear sweep voltametric (LSV) curves of Ag/Sn catalysts in CO_2-saturated and 1 M KOH aqueous solution at a range of 0 V and -1.2 V *vs.* RHE in flow-cell system. (c) Electrochemical impedance spectra (EIS) of Ag/Sn. The Nyquist plots were measured with frequencies ranging from 100 kHz to 0.1 Hz at a potential of -1V *vs.* RHE) in flow-cell system. (d) Stability test at −100 mA cm^{-2} in 1M KOH over 10 h. The bar diagram represents the FE (left y-axis) of CO (red) and H_2 (blue), and the black line represents the cathode potential (right y-axis). (e) CO_2RR in flow cell with electrolyte of 1 M KOH.

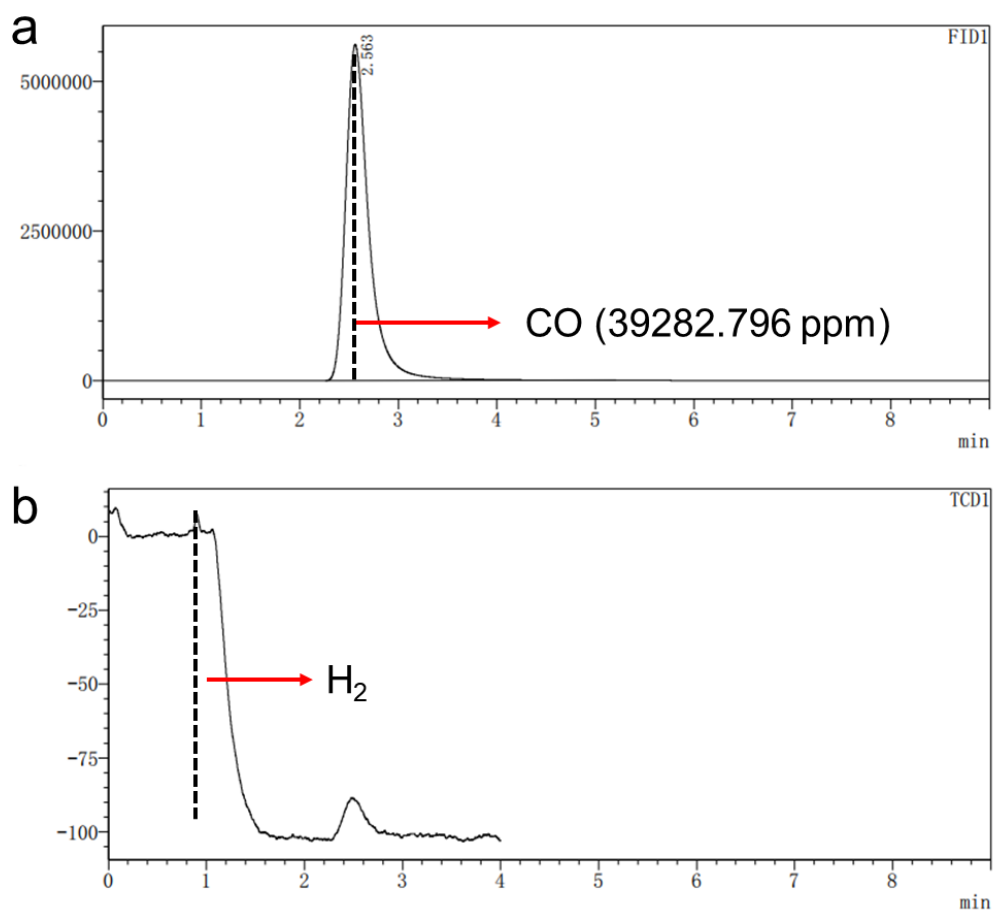**Figure S14 Gas chromatography analysis of Ag/Sn catalyst performance in the GFC system at −100 mA cm⁻² in 1M KOH.** (a) Fid 1 curve image. (b) TCD curve image.
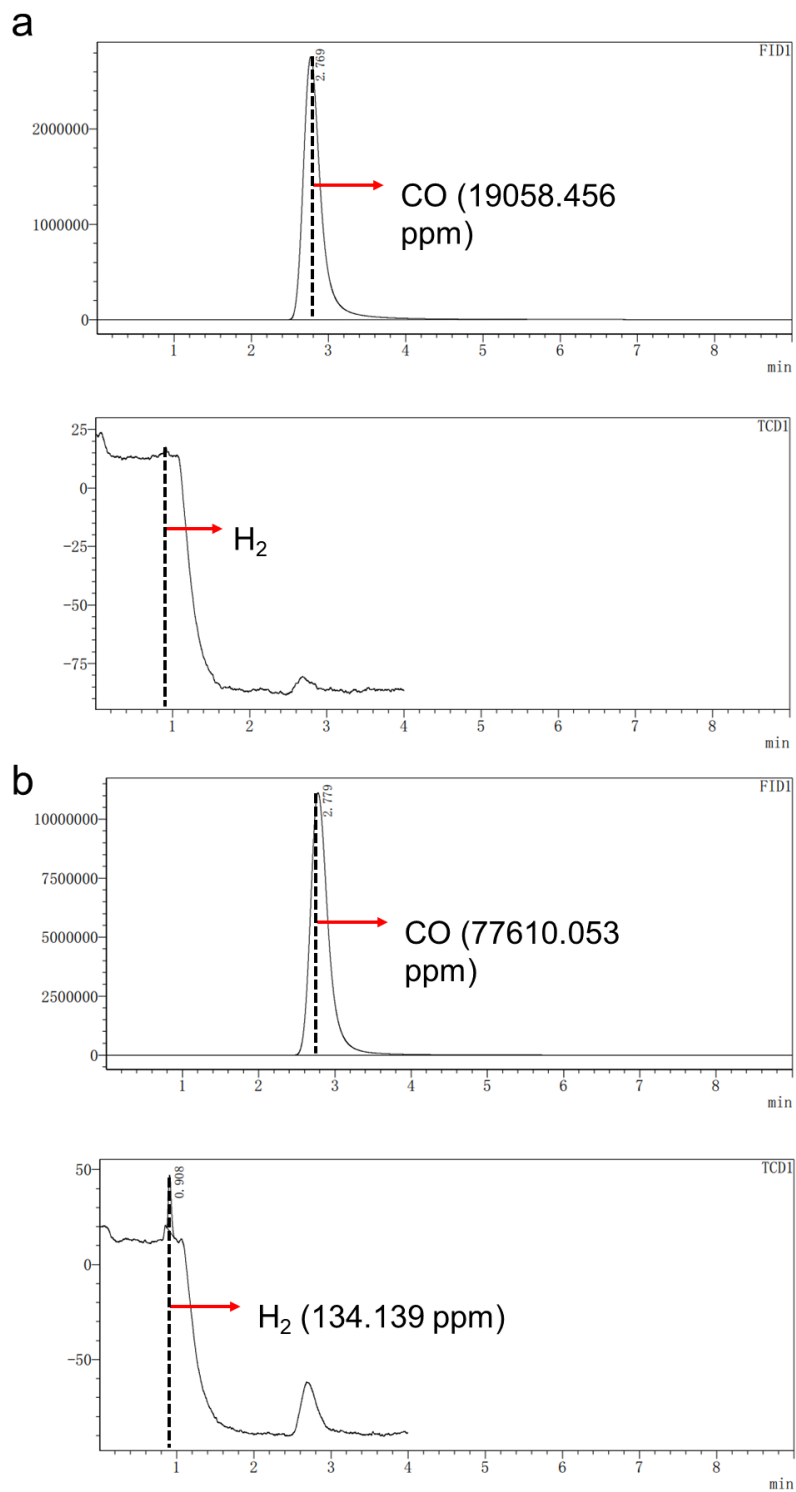
Figure S15 Gas chromatography analysis. (a) Fid 1 and TCD curves for Ag/Sn catalyst performance in the GFC system at −50 mA cm^{-2} in 1M KOH. (b) Fid 1 and TCD curves for Ag/Sn catalyst performance in the GFC system at −200 mA cm^{-2} in 1M KOH.

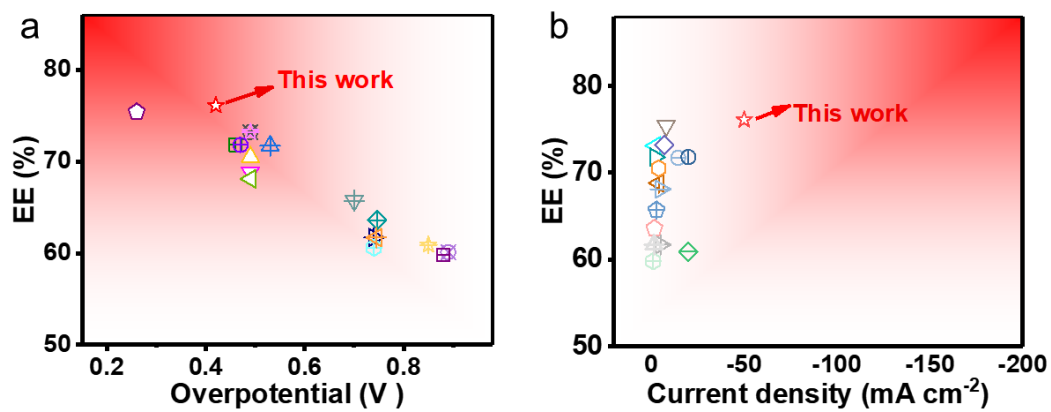**Figure S16 Performance.** Comparison on EE as the function of (a) Overpotential, and (b) Current density of CO. The different symbols indicate the catalysts collected from literatures.
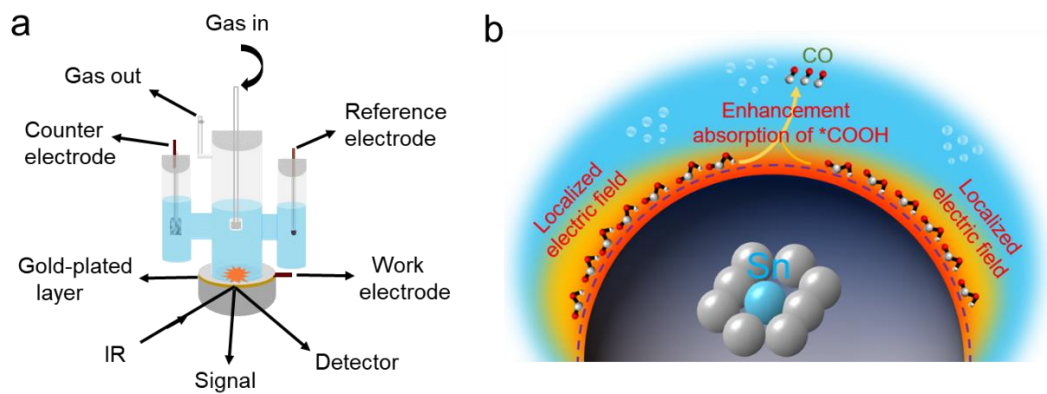
Figure S17 In-situ ATR-IR experiments. (a) Schematic diagram of in-situ ATR-IR. (b) Schematic illustration that the localized electric field enhances the intermediate (*COOH) adsorption by the introduction of Sn atoms.
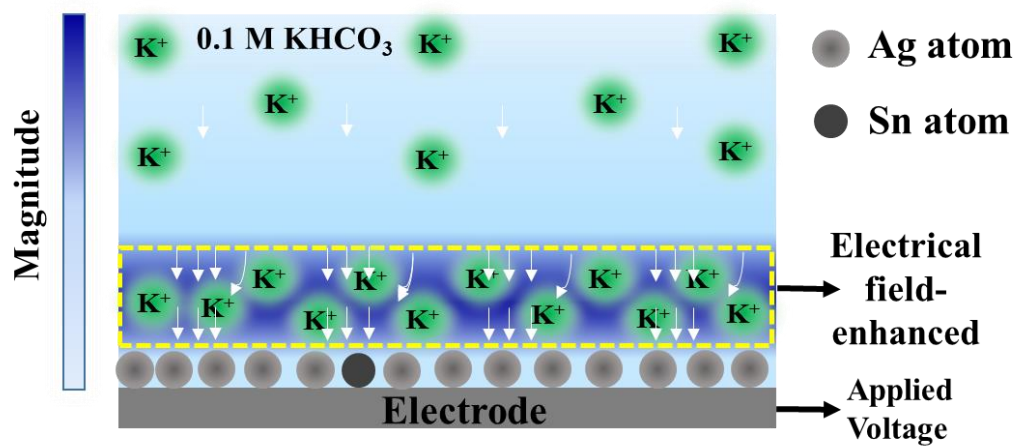
Figure S18 The schematic illustration of K$^+$ adsorbed on catalyst surface under the effect of electric field.

The measurement of K⁺ adsorption capacity. To perform the experience, by using a three-electrode system in 0.1 M $KHCO_3$. The capacity of adsorbed K^+ on electrodes were measured by Ion Chromatograph (IC, Thermo Scientific ICS-600 Ion Chromatography System). As shown in Supplementary Fig.12, the electrodes were run in 0.1M $KHCO_3$ solution at the potential of –0.8 V *vs.* RHE. While running 120 s, the electrode was quickly lifted with voltage above the level of the electrolyte. Following the applied potential of electrode was removed, and the electrode was immersed in 10 ml pure water, shaking for 1 min in pure water to enable the adsorbed K^+ on the surface of catalysts can be completely released into the pure water. Above process was repeated 10 times, then the capacity of K^+ in the water was measured using an Ion Chromatograph.
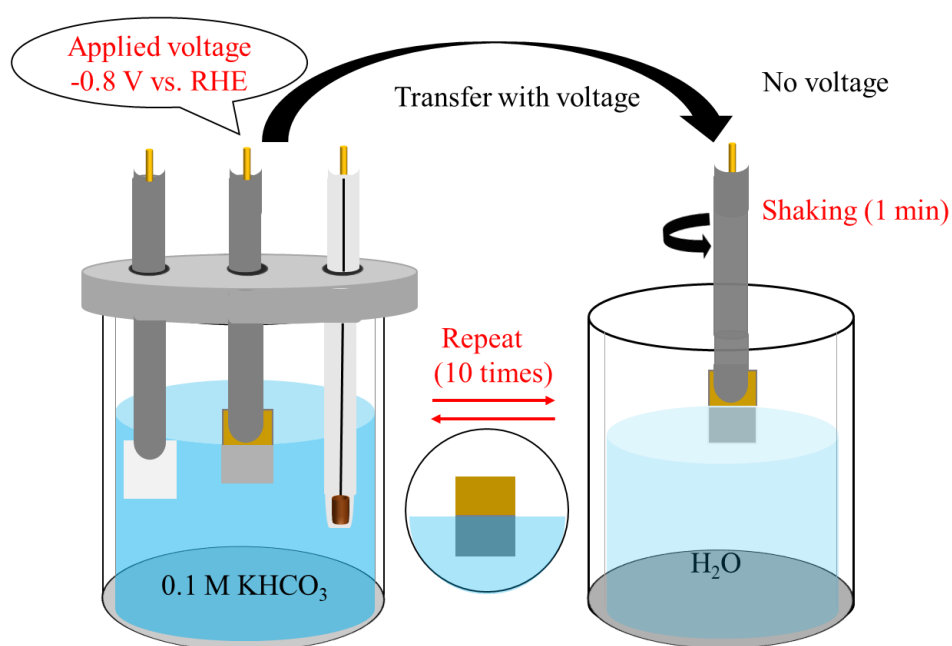
Figure S19 Schematic diagram of K^+ concentration measurement process.
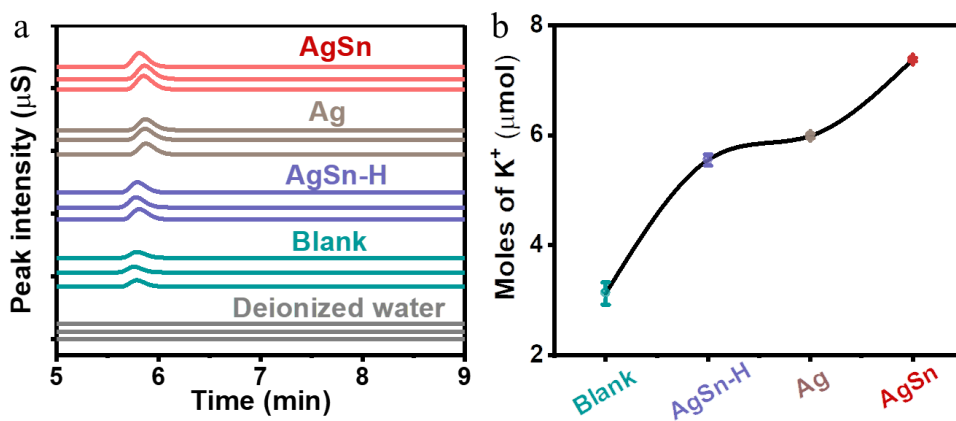
Figure S20 Adsorbed K$^+$ concentration measurement. (a) Results of K$^+$ concentration collected from Ion Chromatograph. (b) Capacity of K$^+$ adsorption on the different electrodes.
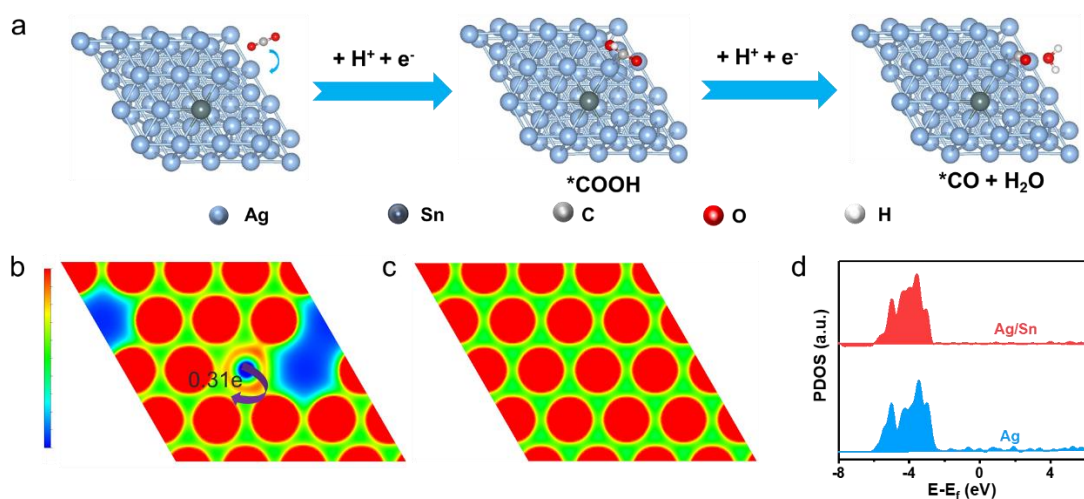
Figure S21 The distribution of charge. (a) Simulation considering the pathway for CO production. (b) Distribution of charge on Ag/Sn catalyst. (c) Distribution of charge on pure Ag catalyst. (d) PDOS of the d-band for Ag/Sn and Ag.
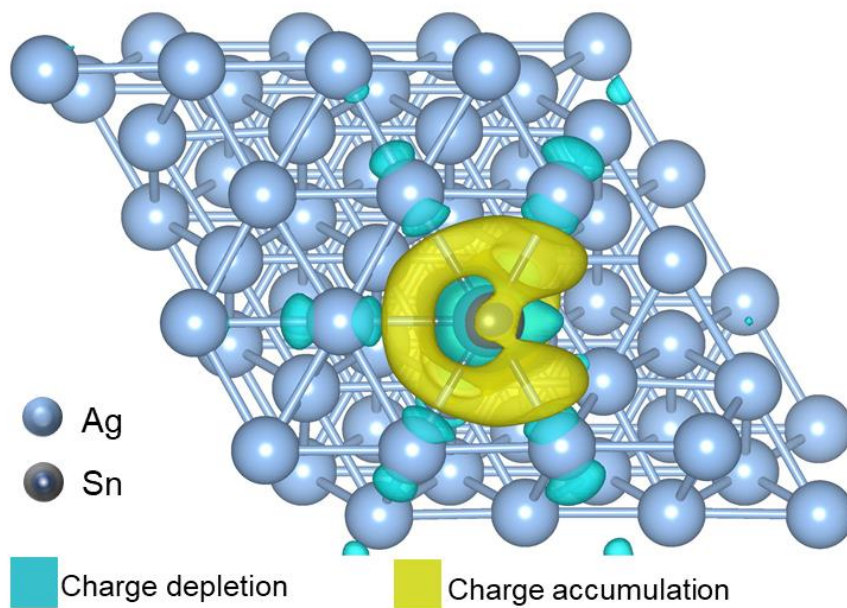
Figure S22 Schematic of calculated charge densities among Ag and Sn atoms.
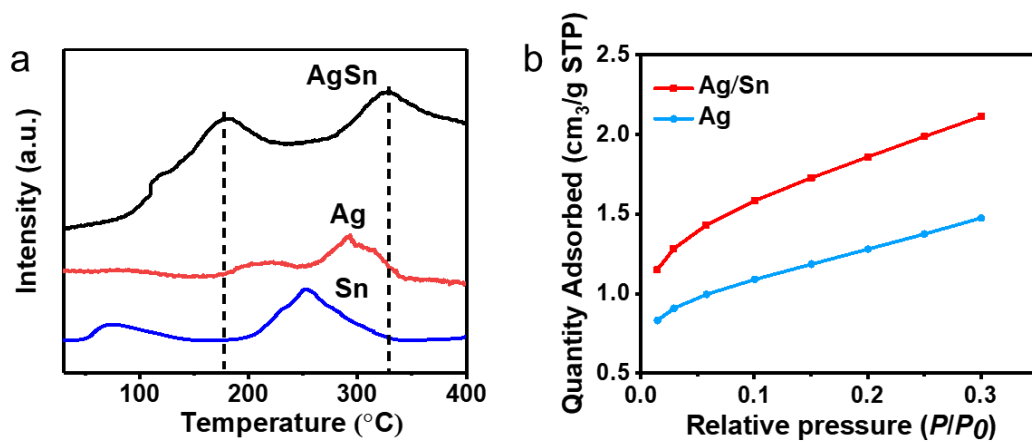
Figure S23 Characterization analysis of catalysts. (a) CO_2 temperature programmed desorption (TPD) tests. (b) N_2 adsorption isotherms.
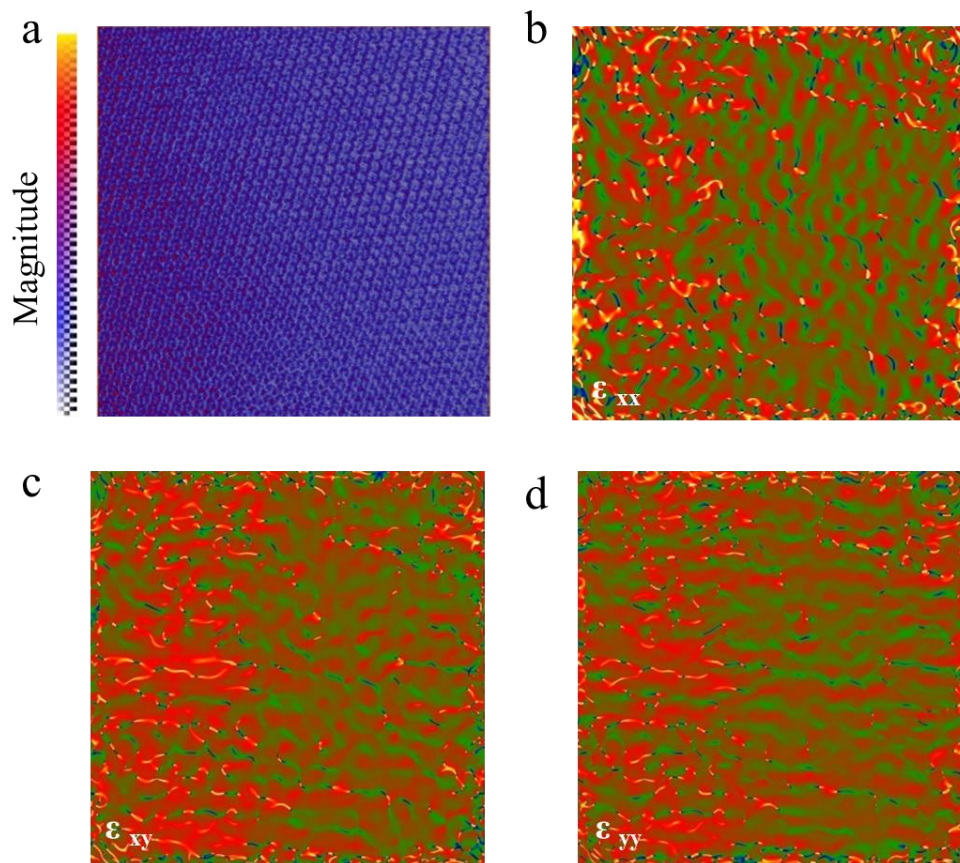
Figure S24 Atomic strain distribution of Ag/Sn. Atomic strain distribution based on (a) HAADF image and corresponding maps of (b) horizontal normal strain ε_{xx}. (c) vertical normal strain ε_{yy} and (d) shear strain ε_{xy}.
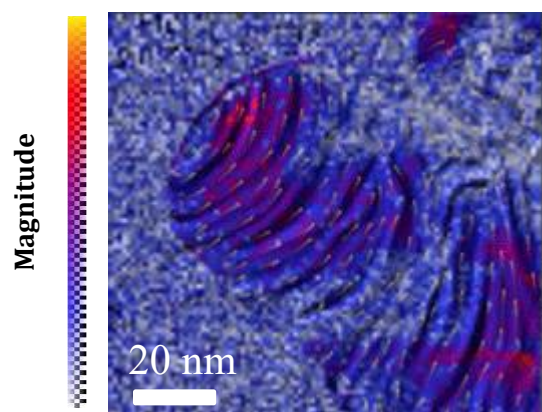
Figure S25. **Electric field dynamic diagram of Ag/Sn**. Arrow-map representations of strength and orientation of electric field.
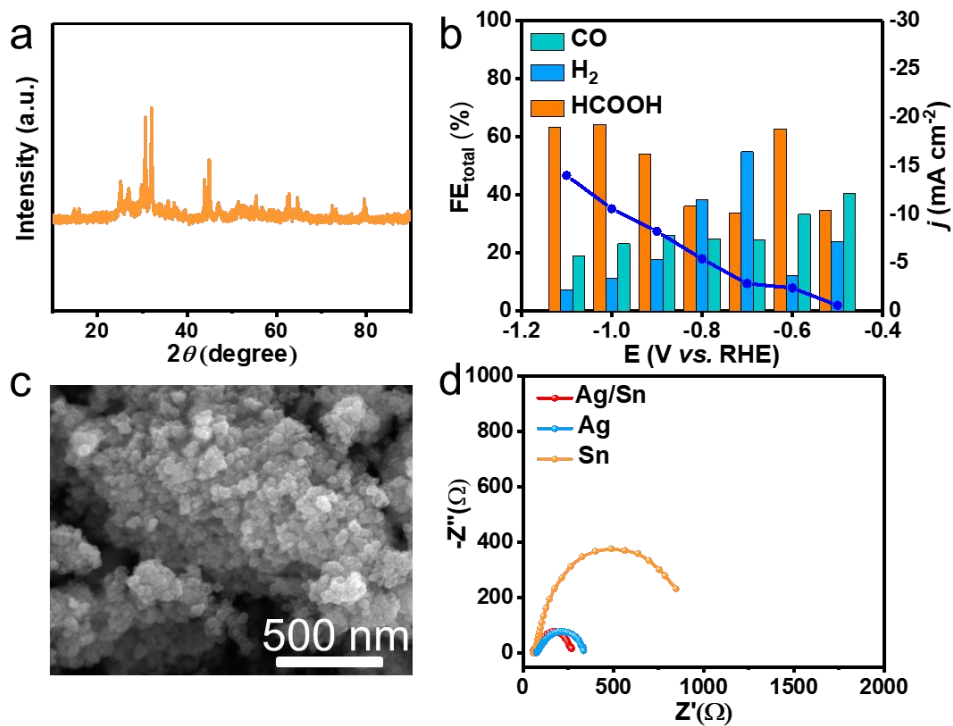
Figure S26 Characterizations and performance of the Sn catalyst. (a) XRD pattern. (b) FEs of H_2, CO, $HCOO^-$ and current density. (c) SEM image. (d) Electrochemical impedance spectra (EIS) of Ag/Sn, Ag and Sn.
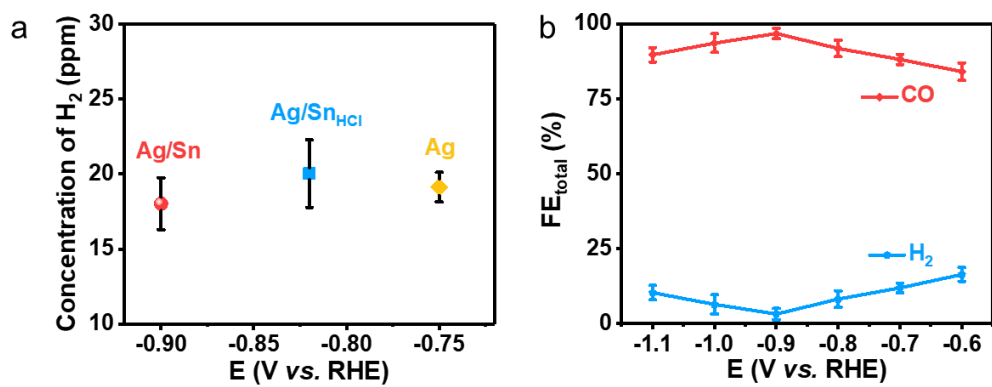
Figure S27 ECR performance. (a) Lowest test potential of HER for catalysts. (b) Low concentration CO_2 (30%) electrochemical reduction reaction for Ag/Sn catalyst.
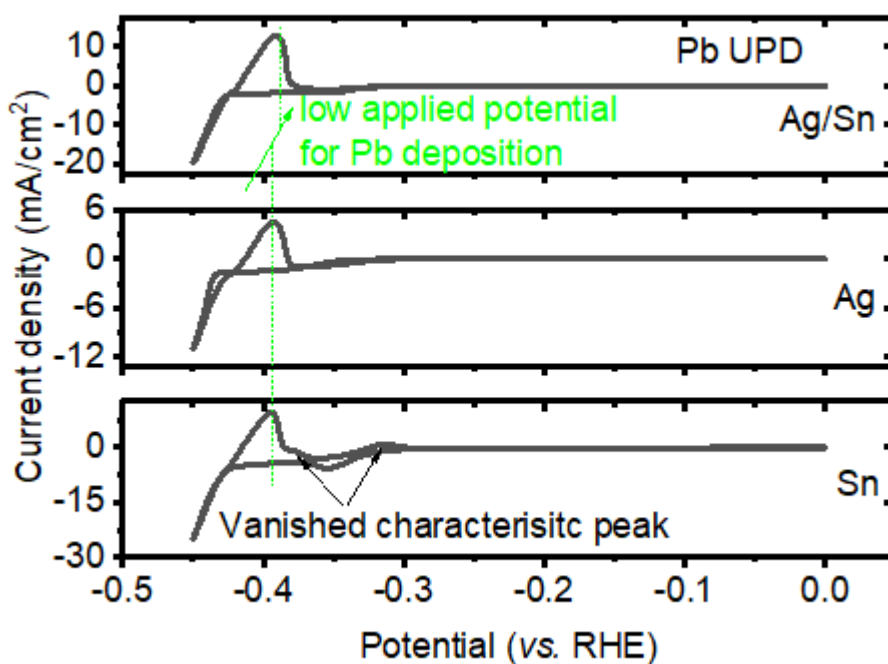
Figure S28 The Pb UPD test. The Pb UPD is conducted at atmosphere in a electrolyte (10 mM KCl, 10 mM $Pb(NO_3)_2$, and 2 mM HNO_3) with a three electrode system. Scan rate is 50 mV/s. The Ag/Sn alloy possesses low potential for Pb deposition, indicating that the reaction barrier on Ag/Sn alloy is lower than Ag and Sn. The characteristic peaks are vanished, demonstrating the Ag is the active sites for reaction. The deposition peak area of Ag/Sn is larger than Ag and Sn, demonstrating that the Sn atoms can highly promote the adsorption ability of surficial Ag during reaction. These results elucidate that the high catalytic activity of Ag/Sn alloy stem from the decreased barrier of reaction and the enhanced adsorption ability of surficial Ag near to Sn atoms.

Table S1. BET area calculation for catalysts from measured nitrogen isotherm at 77 K.

Catalyst	BET Surface Area
Sn-Ag	6.6 m²/g
Ag	4.5 m²/g

Table S2. Various characterization to determine the Sn content in Ag/Sn$_{HCl}$. In all cases, the Sn concentration was below the limit of detection (as expected for the efficient HCl washing step).

	XPS	EDS	ICP
Sn content of Ag/Sn$_{HCl}$	0	0	0

Table S3. Summary of E, *j*, FE and EE for various catalysts in KHCO₃ and KOH electrolyte.

Sample	Electrolyte	E (V *vs.* RHE)	*j* (mA cm⁻²)	FE$_{CO}$ (%)	EE (%)	Cell configuration [a]	ref.
Ag-Sn	0.1 M KHCO₃	-0.6	~2.2	~100	73.2	HC	This work
	1 M KOH	-0.53	50	~100	76.1	FC	
	1 M KOH	-1.21	300	98.9	54.3	FC	
	1 M KOH	-1.36	500	98.0	50.7	FC	
Zn−Ag−O	0.5 M KHCO₃	-0.93	~20	98.1	60.9	HC	[1]
Ag-D	0.1 M KHCO₃	-0.81	~2.8	~100	65.7	HC	[2]
Ag-D	1 M KOH	-1	180	~100	60.1	FC	[2]
2D Silver	0.1 M KCO₃	-0.6	~4	~94	68.8	HC	[3]
Ag₁/MnO₂	0.5 M KHCO₃	-0.85	~5	95.7	61.7	HC	[4]
Au-N	0.5 M KHCO₃	-0.57	~2	96.5	71.8	HC	[5]
Planar silver	0.1 M KHCO₃	-0.99	~1.1	>99	59.8	HC	[6]
M-TTCOFs	0.5 M KHCO₃	-0.8	~3	~99.7	65.8	HC	[7]
L25-Ag-NCs	0.1 M KHCO₃	-0.856	~1.7	99	63.6	HC	[8]
Ag nanofoam	0.5 M KHCO₃	-0.6	~5	~93	68.1	HC	[9]
Porous Ag	0.1 M KHCO₃	-0.85	N.A.	94	60.6	HC	[10]
Pd₁Au₂₄	0.1 M KHCO₃	-0.6	~7	~100	73.2	HC	[11]
NiPc-OMe	0.5 M KHCO₃	-0.64	14.5	100	71.7	HC	[12]
NiPc-CN	1 M KHCO₃	-0.5	50	99.6	77.1	HC	[12]
Fe³⁺−N−C	0.5 M KHCO₃	-0.37	8	~90	75.4	HC	[13]
Ag -CP	1 M KOH	-0.36	25	96	84.3	HC	[14]
A-Ni-NSG	0.5 M KHCO₃	-0.58	~20	97	71.8	HC	[15]
Tri-Ag-NPs	0.1 M KHCO₃	-0.855	~1.5	96.8	61.7	HC	[16]
Au-NN	0.5 M KHCO₃	-0.35	22	>95	81.4	HC	[17]
Au nanowires	0.5 M KHCO₃	-0.35	~3	94	79.7	HC	[18]

[a] HC and FC are short for H-Cell and Flow-Cell, respectively.

Energy efficiency (EE) is calculated according to the following equation [1-2],

$$EE = \frac{E_1 \cdot FE}{E_0 - E_2}$$

E_1 is the thermodynamic equilibrium potential between the anode and cathode reactions ($E_1 = E_0$ - $E_{eq\ cathode}$). E_0 is the thermodynamic equilibrium potential for the anode reaction (i.e. oxygen evolution reaction) equal to 1.23 V (vs. RHE). $E_{eq\ cathode}$ is the thermodynamic equilibrium potential for the cathode reaction ($E_{eq\ cathode,co}$ = -0.11 V, $E_{eq\ cathode,formate}$ = -0.03 V). E_2 is the applied cathode potential.

References

[1] Z. Zhang, G. Wen, D. Luo, B. Ren, Y. Zhu, R. Gao, H. Dou, G. Sun, M. Feng, Z. Bai, A. Yu, Z. Chen, *J. Am. Chem. Soc.* **2021**, *143*, 6855-6864.

[2] X. Wu, Y. Guo, Z. Sun, F. Xie, D. Guan, J. Dai, F. Yu, Z. Hu, Y. C. Huang, C. W. Pao, J. L. Chen, W. Zhou, Z. Shao, *Nat. Commun.* **2021**, *12*, 660.

[3] K. Qi, Y. Zhang, J. Li, C. Charmette, M. Ramonda, X. Cui, Y. Wang, Y. Zhang, H. Wu, W. Wang, X. Zhang, D. Voiry, *ACS Nano* **2021**, *15*, 7682-7693.

[4] N. Zhang, X. Zhang, L. Tao, P. Jiang, C. Ye, R. Lin, Z. Huang, A. Li, D. Pang, H. Yan, Y. Wang, P. Xu, S. An, Q. Zhang, L. Liu, S. Du, X. Han, D. Wang, Y. Li, *Angew. Chem. Int. Ed. Engl.* **2021**, *60*, 6170-6176.

[5] S. F. Yuan, R. L. He, X. S. Han, J. Q. Wang, Z. J. Guan, Q. M. Wang, *Angew. Chem. Int. Ed. Engl.* **2021**, *60*, 14345-14349.

[6] A. Thevenon, A. Rosas-Hernández, A. M. Fontani Herreros, T. Agapie, J. C. Peters, *ACS Catal.* **2021**, *11*, 4530-4537.

[7] H. J. Zhu, M. Lu, Y. R. Wang, S. J. Yao, M. Zhang, Y. H. Kan, J. Liu, Y. Chen, S. L. Li, Y. Q. Lan, *Nat. Commun.* **2020**, *11*, 497.

[8] S. Liu, C. Sun, J. Xiao, J.-L. Luo, *ACS Catal.* **2020**, *10*, 3158-3163.

[9] L. Wei, H. Li, J. Chen, Z. Yuan, Q. Huang, X. Liao, G. Henkelman, Y. Chen, *ACS Catal.* **2019**, *10*, 1444-1453.

[10] S. C. Abeyweera, J. Yu, J. P. Perdew, Q. Yan, Y. Sun, *Nano Lett.* **2020**, *20*, 2806-2811.

[11] S. Li, D. Alfonso, A. V. Nagarajan, S. D. House, J. C. Yang, D. R. Kauffman, G. Mpourmpakis, R. Jin, *ACS Catal.* **2020**, *10*, 12011-12016.

[12] X. Zhang, Y. Wang, M. Gu, M. Wang, Z. Zhang, W. Pan, Z. Jiang, H. Zheng, M. Lucero, H. Wang, G. E. Sterbinsky, Q. Ma, Y.-G. Wang, Z. Feng, J. Li, H. Dai, Y. Liang, *Nat. Energy* **2020**, *5*, 684-692.

[13] C.-S. H. Jun Gu1, Lichen Bai1, Hao Ming Chen2*, Xile Hu1*, *Science* **2019**, *364*, 1091–1094.

[14] R. Wang, H. Haspel, A. Pustovarenko, A. Dikhtiarenko, A. Russkikh, G. Shterk, D. Osadchii, S. Ould-Chikh, M. Ma, W. A. Smith, K. Takanabe, F. Kapteijn, J. Gascon, *ACS Energy Lett.* **2019**, *4*, 2024-2031.

[15] H. B. Yang, S.-F. Hung, S. Liu, K. Yuan, S. Miao, L. Zhang, X. Huang, H.-Y. Wang, W. Cai, R. Chen, J. Gao, X. Yang, W. Chen, Y. Huang, H. M. Chen, C. M. Li, T. Zhang, B. Liu, *Nat. Energy* **2018**, *3*, 140-147.

[16] S. Liu, H. Tao, L. Zeng, Q. Liu, Z. Xu, Q. Liu, J. L. Luo, *J. Am. Chem. Soc.* **2017**, *139*, 2160-2163.

[17] M. Liu, Y. Pang, B. Zhang, P. De Luna, O. Voznyy, J. Xu, X. Zheng, C. T. Dinh, F. Fan, C. Cao, F. P. de Arquer, T. S. Safaei, A. Mepham, A. Klinkova, E. Kumacheva, T. Filleter, D. Sinton, S. O. Kelley, E. H. Sargent, *Nature* **2016**, *537*, 382-386.

[18] W. Zhu, Y. J. Zhang, H. Zhang, H. Lv, Q. Li, R. Michalsky, A. A. Peterson, S. Sun, *J. Am. Chem. Soc.* **2014**, *136*, 16132-16135.